Arabian Journal of Chemistry (2020) 13, 6061–6071

King Saud University

Arabian Journal of Chemistry

www.ksu.edu.sa
www.sciencedirect.com

ORIGINAL ARTICLE

High-efficiency electrodeposition of polyindole nanocomposite using MoS_2 nanosheets as electrolytes and their capacitive performance

Liming Xu [a,1], Danqin Li [a,1], Weiqiang Zhou [a,b,*], Yongbo Ding [a], Yanli Wu [a], Jingkun Xu [a,*], Xuemin Duan [a]

[a] *Flexible Electronics Innovation Institute (FEII), Jiangxi Science and Technology Normal University, Nanchang 330013, PR China*
[b] *Jiangxi Engineering Laboratory of Waterborne Coatings, Jiangxi Science and Technology Normal University, Nanchang 330013, PR China*

Received 1 February 2020; accepted 4 May 2020
Available online 19 May 2020

KEYWORDS

MoS_2;
Polyindole;
Electrodeposition;
Nanocomposites;
Supercapacitor

Abstract Polyindole (PIn) has attracted extensive interest as promising energy storage materials owing to fairly good thermal stability, high redox activity and stability, however, it is challenging to prepare high-quality PIn in neutral solvents by electrochemical method. Herein, a simple route, based on MoS_2 nanosheets as electrolytes, has been developed for the electrochemical preparation of PIn/MoS_2 nanocomposite in acetonitrile solution. Due to the coordination interaction between indole and MoS_2, the onset oxidation potential of indole in this medium was reduced to 0.5 V from 0.75 V determined in acetonitrile/$LiClO_4$. The morphologies and structures of as-obtained PIn/MoS_2 nanocomposite were characterized using SEM, TEM, XRD, Raman and XPS. The results of thermal analysis indicated that the PIn/MoS_2 nanocomposite had an improved thermal stability relative to PIn and MoS_2 nanosheets. Moreover, the specific capacitance of PIn/MoS_2 nanocomposite was 8.3 times higher than that of PIn prepared acetonitrile/$LiClO_4$. To the best of our knowledge, this is the first report on the high-efficiency electrodeposition of PIn/MoS_2 nanocomposite in MoS_2-based acetonitrile solution, which will be a promising candidate as a high efficient electrode material in the application of supercapacitors.

* Corresponding authors at: Flexible Electronics Innovation Institute (FEII), Jiangxi Science and Technology Normal University, Nanchang 330013, PR China (W. Zhou).
E-mail addresses: zhouwqh@163.com (W. Zhou), xujingkun@tsinghua.org.cn (J. Xu).
[1] Liming Xu and Danqin Li contributed equally to this work.
Peer review under responsibility of King Saud University.

Production and hosting by Elsevier

https://doi.org/10.1016/j.arabjc.2020.05.006
1878-5352

1. Introduction

As one of the most important energy storage devices, supercapacitors (SCs) have attracted extensive research due to its higher power density than batteries, as well as advantages including long service life, large power density, fast charging and discharging processes, and environmental protection (Zheng et al., 2017; Wang et al., 2018; Li et al., 2019a; Zhang et al., 2019a; Wang et al., 2019a; Li et al., 2019b; Li et al., 2020). SCs are characterized by storing charges in two ways: (1) The electric double layer capacitance comes from the ion adsorption and desorption at the electrode electrolyte interface (Zhang et al., 2018; Wang et al., 2019b), but its specific capacitance is low; (2) The pseudo-capacitance comes from the reversible faraday reaction that occurs at the electrode/-electrolyte interface (Zhang et al., 2019b; Zheng et al., 2017; Zheng et al., 2018), while its cycle stability is limited. To compensate for their shortcomings, the two mechanisms often work together (Xiao et al., 2019; Wang et al., 2019c). In order to develop high-performance SCs, the electrode materials with high specific capacitance are key. Nowadays, carbon materials (Xiao et al., 2020; Li et al., 2017a), conducting polymers (CPs) (Wang et al., 2020; Cheng et al., 2020) and metal oxygen/sulfides (Huang et al., 2019; Ye et al., 2019; He et al.,2019; Zhang et al., 2017a) are widely studied as electrode materials.

CPs such as polyaniline, polypyrrole, polythiophene and their derivatives along with composites have attracted extensive research interest owing to their desirable physical, chemical and electrochemical properties (Snook et al., 2011; Shi et al., 2015; Xu et al., 2010). Among CPs, polyindole (PIn) has attracted significant attention due to its numerous advantages including rapid electrochromic properties, stable redox properties and high thermal stability (Maarouf et al., 1994; Abthagir et al., 1998). In recent years, PIn has been considered as a potential candidate for applications in electrocatalysis (Zhou et al., 2010), sensors (Tebyetekerwa et al., 2017), lithium batteries (Cai et al., 2013), SCs (Zhou et al., 2016a) and other fields. PIn was synthesized mainly through chemical oxidation and electrochemical oxidation. Presently, there are a few reports on supercapacitance of PIn, in which PIn was prepared only by chemical synthesis method (Cai et al., 2016; Zhou et al., 2016b; Raj et al., 2015; Tebyetekerwa et al., 2017; Majumder et al., 2017). Due to PIn prepared by chemical oxidation is in the form of a powder, the nonconducting binder such as polyvinylidene fluoride needs to be added in the process of electrode preparation, which results in the performance loss of PIn. Alternatively, the electrodeposition is one of the most useful approaches for one-step preparation of CPs electrodes without any binders. The electrodeposition of PIn was mainly carried out in neutral solvents, such as acetonitrile (ACN), benzonitrile, and CH_2Cl_2, with ClO_4^- or BF_4^- as the supporting electrolyte. However, the preparation of PIn in these systems was very difficult and its properties were not very good (Xu et al., 2005). Boron trifluoride diethyl etherate (BFEE) has been used to prepare free-standing PIn film because the catalytic effect of BFEE and the interaction between BFEE and aromatic monomers can reduce the oxidation potential of monomers (Xu et al., 2005). However, the middle strong Lewis acid, BFEE, is unsafe to human body in that it breaks down into HF in the air, and it is not environmentally friendly because of its toxicity. Therefore, it is important to look for better methods to prepare the high-quality PIn by the electrodeposition method.

Similar to graphene, MoS_2 nanosheet has obtained more and more attention because of its unique structure and electronic characteristics, such as large specific surface area, good biocompatibility and electrochemical properties (Gan et al., 2017; Dey et al., 2013; Thangappan et al., 2016). In MoS_2 crystal, the Mo layer is sandwiched between two S layers, and the Mo atoms in the intermediate layer have an oxidation state range from +2 to +6 (Ji et al., 2015; Li et al., 2017b; Huang et al., 2017). So MoS_2 shows pseudo-capacitance like transition metal oxides such as RuO_2 and MnO_2 (Huang et al., 2018). Currently, although some composites based on PIn and metal oxides (MnO_2, V_2O_5 and Co_3O_4) have been prepared such as MnO_2/poly-5-cyanindole (Zhou et al., 2014), V_2O_5/PIn/carbon cloth (Zhou et al., 2016c), and Co_3O_4/PIn (Raj et al., 2015), there are shortcomings in these works due to below reason: We know that MnO_2, V_2O_5 and Co_3O_4 show good electrochemical behaviors in basic solution or neutral aqueous solution, but they have poor redox activity in acidic electrolyte. However, PIn can show excellent redox activity in acidic electrolyte, whereas its electrochemical activity is very poor in basic solution or neutral aqueous solution. Therefore, in terms of the beneficial synergistic effects, the construction of the above mentioned composites is defective because of sacrificing the excellent electrochemical activity of PIn. So it is very significant to rationally design a nanocomposite material by incorporating MoS_2 with high electrochemical behaviors in acidic aqueous solution into PIn, which will maximize the synergistic effects between MoS_2 and PIn.

Analogously to the function of BFEE, MoS_2 nanosheets with negative charges can serve as the supporting electrolyte, and it has been also used as catalyst in the organic synthesis (Yang et al., 2003; Ting et al., 1992; Delmon and Dallons, 1998), for example, the hydrogenolysis of thiophene, pyrrole and furan on MoS_2 or WS_2 catalysts (Delmon and Dallons, 1998). Considering the catalytic effect, when MoS_2 nanosheets are used as electrolytes for the electro-polymerization of indole, it may show unexpected effects. In this study, the electro-polymerization of indole readily occurred in ACN solution using MoS_2 nanosheets as electrolytes. The morphology, structure and thermal stability of as-obtained PIn/MoS_2 nanocomposite were studied. Additionally, it was found that PIn/MoS_2 nanocomposite had better electrochemical properties and stability compared with PIn prepared from other conventional system. We believe that MoS_2 nanosheets as good electrolytes will be extended to the electrochemical preparation of other CPs such as polyaniline, polypyrrole, polythiophene and their derivatives.

2. Experimental

2.1. Chemicals

MoS_2 nanosheets were prepared according to our previous work (Li et al., 2017b). Lithium perchlorate ($LiClO_4$) was purchased from Xiya Reagent Research Center. Indole monomer, acetonitrile (ACN, 99.9%, ACS/HPLC Certified), *n*-butyllithium (1.6 M solution in hexanes) and *n*-hexane (97.5%, SuperDry) were all bought from J&K Chemical Ltd. Doubly distilled water and anhydrous ethanol were used

throughout the work. Other reagents are analytical grade and used directly without further purification unless otherwise noted.

2.2. Preparation of PIn/MoS_2 nanocomposite

MoS_2 nanosheet dispersion was firstly prepared by ultrasonic dispersion in ACN solution. In brief, 45 mg MoS_2 nanosheets were added into 30 mL ACN, followed by sonication (40 kHz, 600 W) for 1 h. In addition, the solution was allowed to stand for one day to remove the settled MoS_2 nanosheets, and the upper dispersion was decanted. So, a homogeneous and stable MoS_2 dispersion (Fig. S1) was achieved, with the resulting concentration estimated to be 0.8 mg mL^{-1} (10 mM). The thickness of exfoliated MoS_2 nanosheet was about 1.3 nm (Fig. S2).

For the electrodeposition of PIn/MoS_2 nanocomposite, a common three-electrode system was adapted. The glass carbon electrode (GCE, Wuhan Gaoss Union Technology Co., Ltd, 0.07 cm^{-2}) was used as the working electrode. Prior to each experiment, its surface should be carefully polished and thoroughly cleaned. The platinum (1.0 mm diameter) and Ag/AgCl were used as counter electrode and reference electrode, respectively. The ACN solution containing 50 mM indole and 10 mM MoS_2 was purged with nitrogen before polymerization to remove oxygen from solution and keep a certain nitrogen pressure. The nanocomposite film was grown potentiostatically on GCE substrates at 1.2 V. Scheme 1 shows the schematic representation of synthesis process. For comparision, PIn was also prepared from the ACN solution containing 50 mM indole and 10 mM $LiClO_4$. Besides, to obtain a sufficient amount of PIn and PIn/MoS_2 nanocomposites for characterization, an ITO-coated glass (2.5 cm × 2 cm) was employed as the working electrode and another one (3 cm × 3 cm) was used as the counter electrode, which was cleaned with ITO detergent, deionized water, acetone and isopropanol for 20 min each time under ultrasonication before using.

2.3. Characterization

The scanning electron microscope (SEM, JSM-5600, JEOL) and transmission electron microscopy (TEM, Tecnai-G20, USA) were used to characterize the morphologies of samples. Raman spectroscopy (Renishaw inVia 2000, UK) was adopted with an incident wavelength of 514 nm and a test range of 50 to 4000 nm. X-ray diffraction (XRD) was tested on the Bruker D8 instrument using CuKα radiation. Thermogravimetric analysis (TGA) was tested on TA Instruments (Q50) to characterization of thermal stability of materials. X-ray photoelectron spectroscopy (XPS, K-Alpha, USA) with Al Ka X-ray radiation as the X-ray source for excitation was carried out to analyze the elemental composition of the complex. The electrochemical properties tests of all electrodes, including cyclic voltammetry (CV), galvanostatic charge/discharge (GCD), cycle stability and electrochemical impedance spectroscopy (EIS) were measured by CHI660E electrochemical analyzer (Shanghai, China) at room temperature. Details regarding the specific capacitance calculations are presented in the Supporting information.

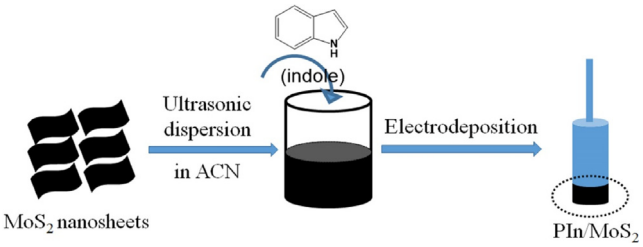

Scheme 1 Schematic diagrams of the electrochemical deposition of PIn/MoS_2 nanocomposite.

3. Results and discussion

High-quality PIn film was difficultly prepared by the electrochemical polymerization of indole monomer in neutral solvents. Fig. 1 shows the anodic polarization curves of 0.1 M indole in ACN solution containing 10 mM $LiClO_4$ and 10 mM MoS_2 at 100 mV s^{-1}, respectively. The onset oxidation potential of indole in ACN/MoS_2 solution was only 0.5 V, which was lower than that determined in ACN/$LiClO_4$ (0.75 V). The lower onset oxidation potential was probably ascribed to the formation of complexes between the monomer and the MoS_2 by a coordinatively unsaturated Mo with its heteroatom N interacting (Delmon and Dallons, 1998; Bazzaoui et al., 1994). The lower potential would provide considerably milder polymerization condition and be in favor of yielding a high-quality polymer.

The successive CV curves of indole monomer were shown in Fig. 2. In ACN solution containing 10 mM $LiClO_4$, the strong anodic current density of the monomer was found in the potential range from about 0.8 to 1.2 V (Fig. 2A), which was the formation of the monomer radical cations and polymer (Mo et al., 2015). However, the peak current density of polymer between 0.2 V and 0.7 V was increased very slow and almost coincide (Fig. 2A, insert). Additionally, only a small amount of polymer was observed on the surface on electrode. This implied the electrochemical polymerization of indole in ACN solution containing 10 mM $LiClO_4$ was not successful. However, as shown in Fig. 2B, the peak current intensity of polymer prepared from ACN solution containing 10 mM MoS_2 was intensified as each successive scan increased, indicating that the product was gradually deposited on the surface of the working electrode with increasing the thickness of polymer. An apparent polymer film was observed by naked eyes. The higher peak current densities and the larger increasing interval reflected a comparatively faster coupling of cation radicals to polymers, suggesting that MoS_2 nanosheets were more efficient electrolytes for producing PIn films.

The morphology of the polymer has a great influence on its electrochemical performance. Therefore, the surface morphology of PIn/MoS_2 nanocomposite was investigated by SEM, as shown in Fig. 3. It can be seen from Fig. 3A, the surface of PIn prepared from ACN solution containing 10 mM $LiClO_4$ was very compact. In Fig. 3B&C, the PIn/MoS_2 nanocomposite was loose and porous, and this morphology not only provided a larger specific surface area for electrochemical generation, but also facilitated the transmission of electrons and enhanced the utilization rate of electrode materials. The effective surface areas of PIn and PIn/MoS_2 electrodes were also tested by CV

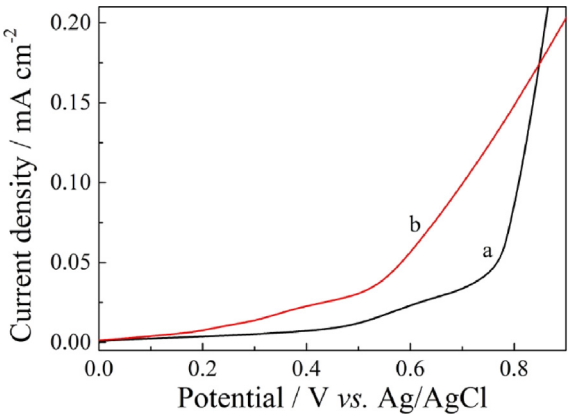

Fig. 1 Anodic polarization curves of 0.1 M PIn in ACN solution containing 10 mM $LiClO_4$ (a) and 10 mM MoS_2 (b) at 100 mV s^{-1}, respectively.

with 5 mM $K_3Fe(CN)_6$ as a probe at different scan rates (Fig S3). The effective surface areas of PIn/MoS_2 electrodes was 0.23 cm^2, which was larger than that of PIn electrode (0.11 cm^2). Besides, the composition of as-prepared PIn/MoS_2 was demonstrated by energy dispersive X-ray (EDX) and elemental mapping analysis. As shown in Fig S4, the C, N, Mo and S atoms were evidenced in the nanocomposite, indicating MoS_2 has been doped in the PIn. And the atomic ratio of Mo to S element ranged from 1.12% to 2.22%, approaching the theoretical value of MoS_2. The EDX mapping analysis (Fig. 3D) demonstrated the uniform distribution of the C, N, Mo and S elements in nanocoposites.

Fig. 4 shows TEM and HRTEM images of as-prepared PIn/MoS_2 nanocomposite. In Fig. 4A, the nanocomposite contained MoS_2 as black part and PIn as light color part. From HRTEM images (Fig. 4B), there were obvious lattice fringes of MoS_2. The lattice fringes spacing corresponded to the layer spacing of the MoS_2. It was found that the interlayer distance of MoS_2 was enlarged from 0.63 nm to 0.68 nm. This may be due to the fact that under the action of electrostatic interaction, the indole nitrogen cations formed during the electropolymerization tended to bind to the MoS_2 layer and adsorb on the surface of the MoS_2 nanosheets (Kim et al., 2016; Yang et al., 2016), which weakened the van der Waals force between the MoS_2 nanosheets, causing the interlayer distance of the MoS_2 nanosheets to increase. This also indicated that the interaction between MoS_2 and PIn not only makes the morphology of PIn more loose and rough, but also increased the layer spacing of MoS_2 nanosheets, which was beneficial to increase the specific surface area of the material and the transmission path of electrolyte ions, and improve the efficiency of ion diffusion, thereby maximizing the capacitive performance of the electrode materials.

Fig. 5 shows the XRD patterns of PIn, MoS_2 and PIn/MoS_2 nanocomposite. A broad band between 15° and 30° was observed from the XRD pattern of PIn. The XRD pattern of MoS_2 nanosheets showed several peaks at 14.2°, 32.9°, 39.6°, 43.9°, 49.6° and 58.8°, respectively, corresponding to the (0 0 2), (1 0 0), (1 0 3), (0 0 6), (1 0 5) and (1 1 0) crystalline planes (Kathiravan et al., 2019). For the XRD pattern of PIn/MoS_2 nanocomposite, it included the information of PIn and MoS_2 nanosheets such as a broad band between 15° and 30°, (0 0 2), (1 0 0), (0 0 6), (1 0 5) and (1 1 0) planes. This indicated the formation of the PIn/MoS_2 nanocomposite.

Raman spectroscopy technique might give more structure information for the MoS_2, PIn and PIn/MoS_2 nanocomposite, and therefore the Raman spectra of the related samples were tested and shown in Fig. 6. The MoS_2 nanosheets showed two characteristic peaks at 383.8 and 406.8 cm^{-1}, respectively, corresponding to the in-plane E^1_{2g} mode vibration caused by the in-plane vibration of Mo atom and S atoms in opposite directions and A_{1g} mode vibration related with the out-of-plane vibration of only S atoms in opposite directions (Kim et al., 2016; Li et al., 2012). Due to the E^1_{2g} and A_{1g} modes are very sensitive to thickness of the MoS_2 sample, the layer number can be determined by measuring frequency difference between E^1_{2g} and A_{1g} modes (Lee et al., 2010; Zhan et al., 2012). The frequency difference of as-prepared MoS_2 nanosheets was 23 cm^{-1}, which was in accordance with that of the double-layered MoS_2 (Zhan et al., 2012). This further indicated that double-layered MoS_2 nanosheet was successfully prepared. Compared to MoS_2, the E^1_{2g} and A_{1g} peaks of PIn/MoS_2 nanocomposite were located at 386.3 and 410.8 cm^{-1}, and the frequency difference was measured to 24.5 cm^{-1}. The reasons for the red shift and the widening of the frequency difference were as follows: (1) the embedded PIn in MoS_2 enlarged the interlayer distance; (2) the PIn on MoS_2 nanosheets increased the thinkness of PIn/MoS_2

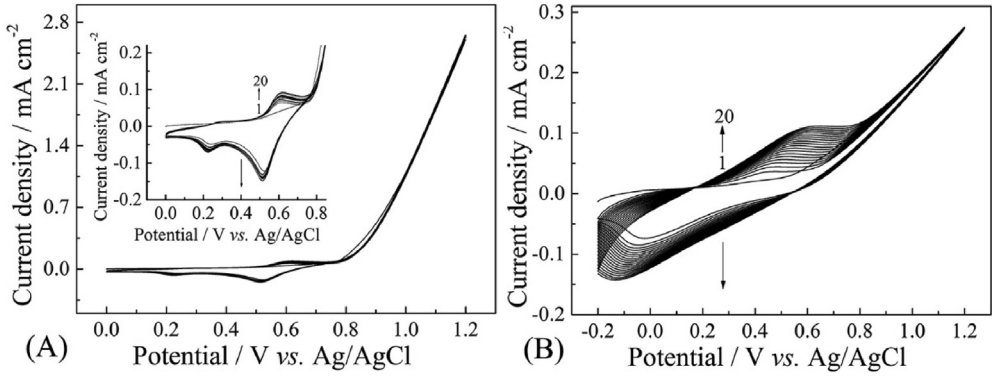

Fig. 2 Successive CV curves of 0.1 M PIn in ACN solution containing 10 mM $LiClO_4$ (a) and 10 mM MoS_2 (b) at 100 mV s^{-1}, respectively.

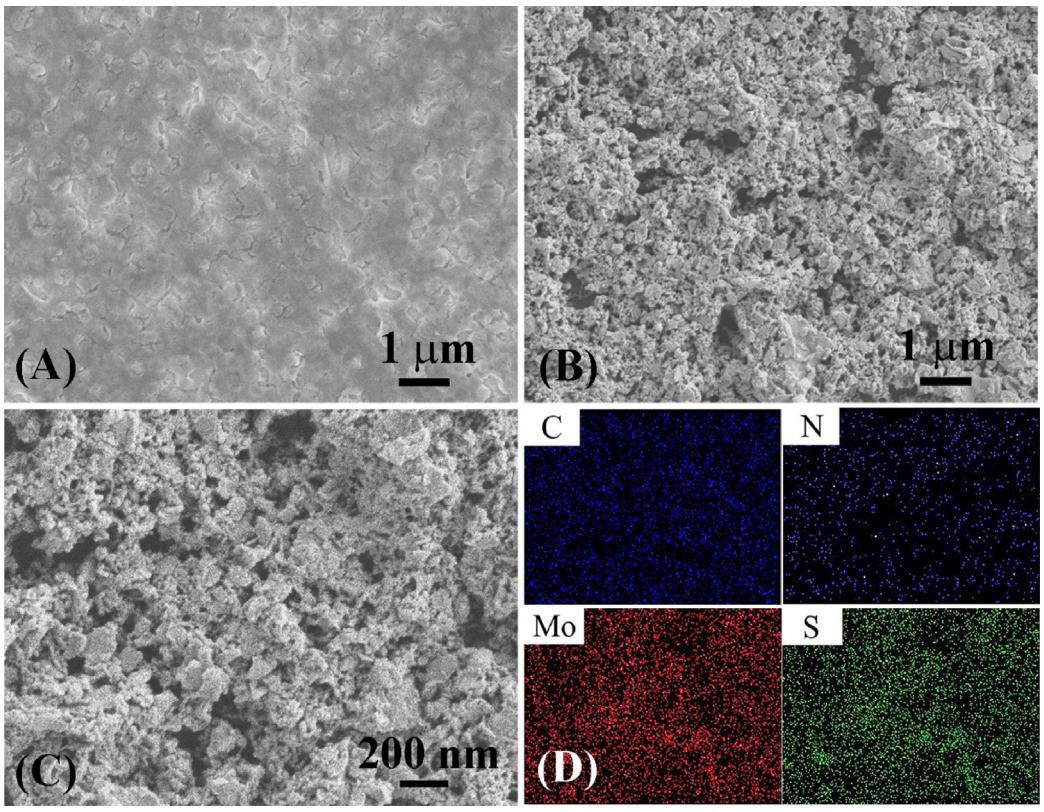

Fig. 3 SEM image of PIn (A) and PIn/MoS_2 nanocomposite (B, C), elemental mapping (D) of the C, N, Mo and S elements for the PIn/MoS_2 nanocomposite.

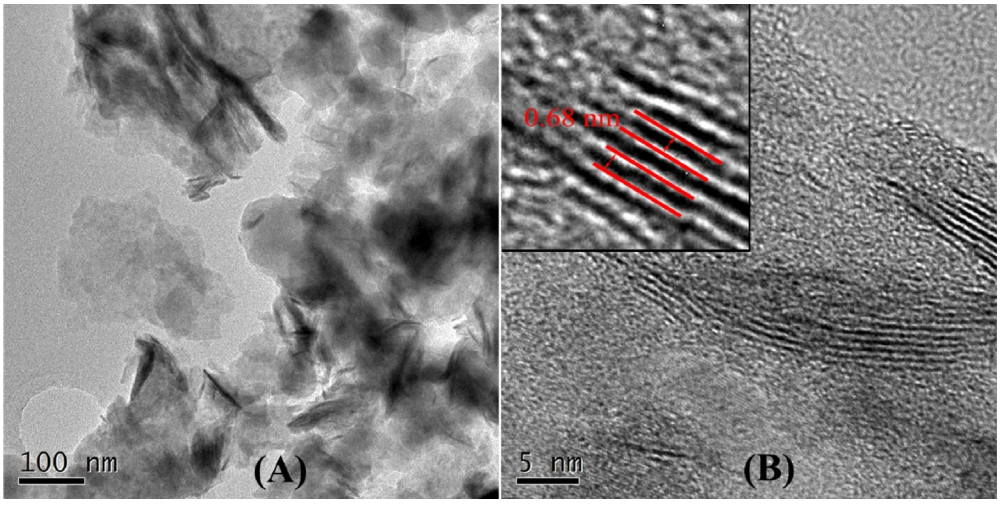

Fig. 4 TEM (A) and HRTEM (B) images of PIn/MoS_2 nanocomposite.

nanocomposite. Besides, the two bands of PIn at about 1339.5 and 1591.3 cm^{-1} were ascribed to the stretching vibrations of pyrrole ring and phenyl ring (Majumder et al., 2017), which appeared for the PIn/MoS_2 nanocomposite. This implied that the PIn/MoS_2 nanocomposite was successfully obtained.

The surface composition and bonding information of the electrodeposited PIn/MoS_2 nanocomposites were explored via XPS. Firstly, a survey scan of the nanocomposite was recorded and presented in Fig. S5. XPS survey spectrum indicated that the nanocomposite contained O, C, N, Mo and S elements. The high resolution XPS patterns of the C, N, Mo and S regions were shown in Fig. 7. In Fig. 7A, the core level spectrum of C1s had four different peaks at 291.48, 285.58, 284.88 and 284.38 eV, respectively, corresponding to C≡N, C═N, C—N and C—C bonds. Specifically, the small peak observed at 291.48 eV was assigned to π–π interaction, implying the existence of interfacial interaction between PIn and MoS_2 (Cai et al., 2016). In Fig. 7B, the N1s curve showed three

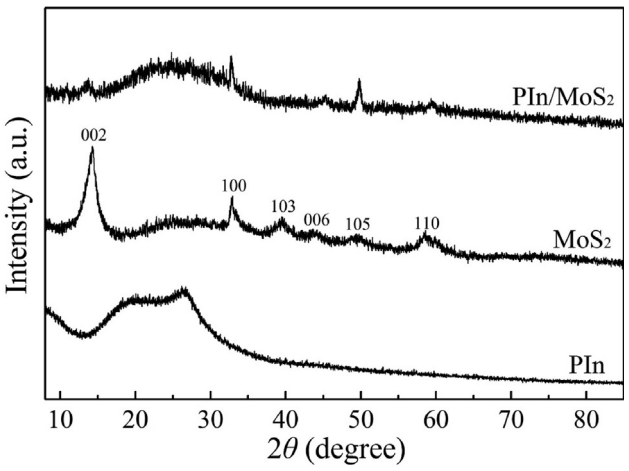

Fig. 5 XRD patterns of PIn, MoS_2 and PIn/MoS_2 nanocomposite.

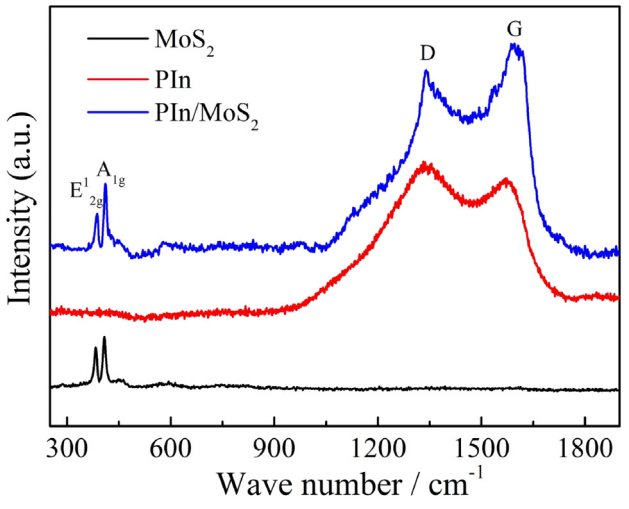

Fig. 6 Raman spectra of PIn, MoS_2 and PIn/MoS_2 nanocomposite.

peaks at 400.48, 399.98 and 396.68 eV, revealing the presence of the —C═N—H, N—H and —C—N. The XPS spectrum of Mo 3d was decomposed into three peaks at 229.48, 232.98 eV and the additional S 2s state at 226.48 eV (Fig. 7C). The S 2p broad peaks, as represented in the Fig. 7D, could be fitted with the split doublet $S_{p3/2}$ and $S_{p1/2}$ located at 162.38 and 163.58 eV, respectively. Besides, there were obviously peaks at 236.18 and 169.48 eV, which were ascribed to Mo^{6+} of Mo $3d_{5/2}$ and S^{6-} of S $2p_{3/2}$, respectively.

The thermal stability of electrode materials is an important factor to judge its application potential. In Fig. 8, the degradation from 100 to 235 °C for MoS_2, PIn and PIn/MoS_2 nanocomposite was about 3%, which was attributed to the evaporation of physically adsorbed water; and between 235 and 440 °C, the mass loss for MoS_2 was about 9%, which was the loss of chemisorbed water (Thangappan et al., 2016). For PIn, the mass was continuously declined, the loss reached 22%, which was due to the degradation of oligomers, other moisture trapped in PIn, and PIn backbone (Zhou et al., 2016b). From 440 to 600 °C, there was a degradation of 17% for MoS_2, this was ascribed to the oxidation of MoS_2 to molybdenum oxide and SO_2 (Thangappan et al., 2016), however, the oxidation of MoS_2 was well inhibited when PIn was introduced, this was due to the strong interactions between MoS_2 and PIn. At the same time, the stability of PIn/MoS_2 nanocomposite was higher than that of PIn, indicating that the nanocomposites had better thermal stability.

The quality of the CPs film prepared by electrochemical methods depends strongly on various experimental parameters, such as the substrate, the solvent, the concentration of the monomer and the applied potential (Shi et al., 1995). In order to get the optimal deposition conditions of PIn/MoS_2 nanocomposite in the following work, the mole percent between indole and MoS_2 and electrodeposition potentials were optimized. As seen from Fig. 9A, the specific capacitance of PIn/MoS_2 nanocomposite reached the maximum value when the molar fraction of MoS_2 was 16%. Generally, at an applied potential was lower than the onset oxidation potential, the polymerization of monomer does not occur. However, once the applied potential reasonably excesses the onset oxidation potential, the polymer film can be formed on the working electrode. Fig. 9B exhibits the chronoamperometry curves of 50 mM indole in ACN solution containing 10 mM MoS_2 at different voltages for 800 s, respectively, which showed a tendency to become constant after a brief descent. The constant current density meant the uniform deposition of the polymer on the electrode surface. When the applied voltage was higher than 1.5 V, some oligomers were dissolved into the solution. This was possibly due to the disequilibrium between the polymerization rate and diffusion rate of monomers. Therefore, the optimized potential of 1.2 V was selected to prepare the PIn/MoS_2 nanocomposite.

Fig. 10 shows the electrochemical performance of PIn and PIn/MoS_2 nanocomposite. From Fig. 10A, the CV curve of PIn showed two redox peaks, while the CV curve of PIn/MoS_2 had four redox peaks, which was derived from the reversible redox reaction of PIn (Majumder et al., 2017; Zhou et al., 2016b) and MoS_2 (Kim et al., 2016) in 1 M H_2SO_4, as shown in Scheme 2. It can be seen that the CV area of PIn/MoS_2 was larger than those of PIn and MoS_2 (Fig. S6), which proved that the nanocomposite had a higher specific capacitance. Fig. 10B&C present the CV curves of PIn and PIn/MoS_2 at different scan rates. During the increase of the scan rate, the peak current density also increased, and the shape of the CV curves did not obviously change, and this meant that the electrode material had a good rate ability. As seen from Fig. S7A, the $R^2 \approx 1$ indicated the current densities of redox peaks were increased linearly as the scan rates increased from 30 to 250 mV s^{-1}. According to the formula: $i = av^b$ (i is the current density and v is the scan rates), when $b = 1$ presented pseudocapacitive behavior (Simon et al., 2014), and the electrochemical behavior of PIn/MoS_2 electrode was an adsorption controlled process. Meanwhile, the relationship between redox peak currents densities and the square root of scan rates was nonlinearly (Fig. S7B), indicating no diffusion process happened (Wang et al., 2016a).

The GCD tests were conducted to further evaluate the performance of the electrode materials. In Fig. 10D&E, the nonlinear GCD curves demonstrated the pseudocapacitive behavior, which was in good agreement with the observed redox peaks in their CV curves. An IR drop was observed for PIn, which was larger than that PIn/MoS_2. This was due

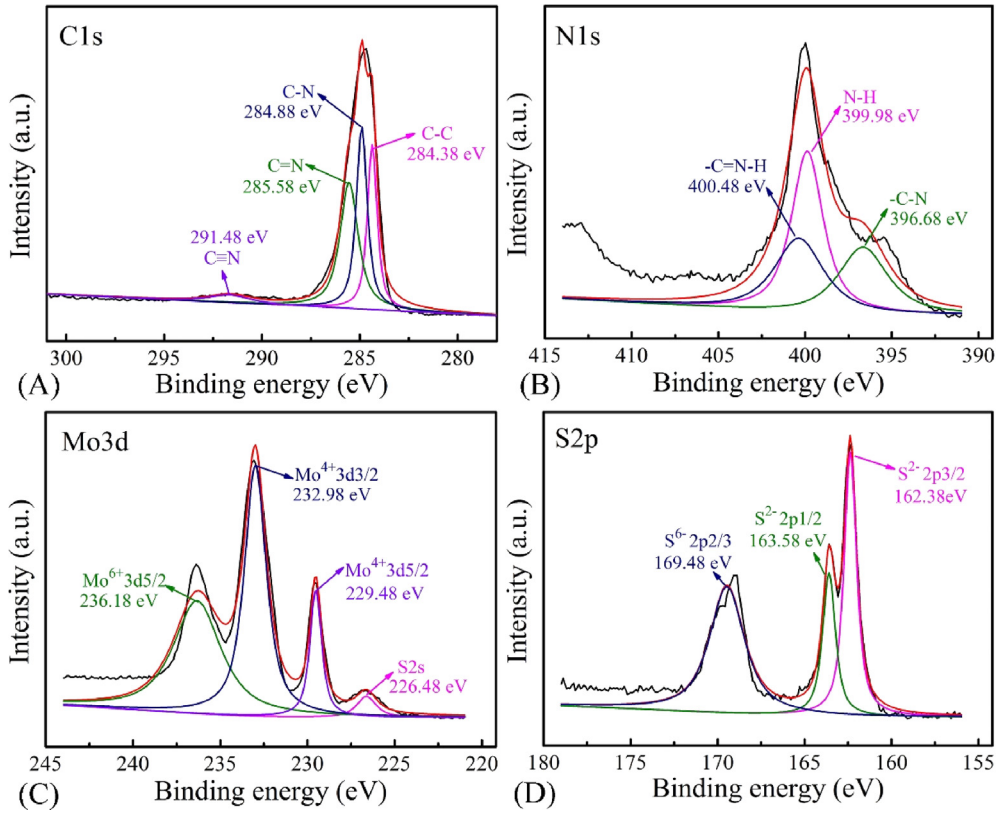

Fig. 7 XPS spectra images of PIn/MoS_2 nanocomposite, (A) C 1s, (B) N 1s, (C) Mo 3d and (D) S 2p.

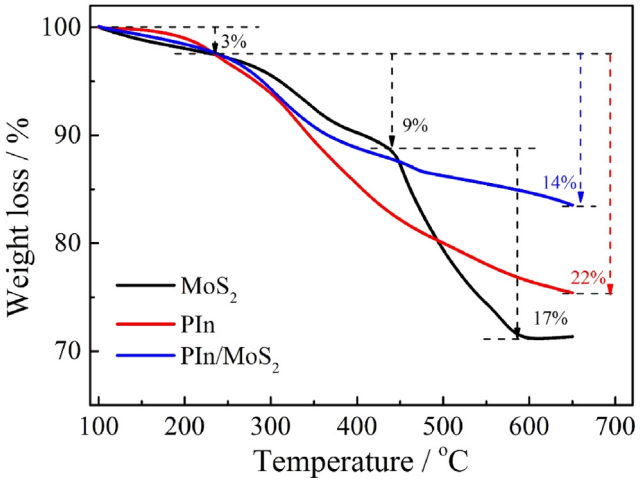

Fig. 8 TGA curves of MoS_2, PIn, and PIn/MoS_2 nanocomposite.

to the small inner resistance of ion diffusion within PIn/MoS_2. The low resistance of nanocomposite film was demonstrated by below electrochemical impedance (EIS). As shown in Fig. 10F, the specific capacitances of PIn/MoS_2 was 35 mF cm^{-2} at 0.3 mA cm^{-2}, which was 8.3 times higher than that of PIn (4.2 mF cm^{-2}). The enhanced performance could be attributed to the porous structure of PIn/MoS_2 and the synergistic effect between MoS_2 and PIn. When the current density was increased to 1.5 mA cm^{-2}, the specific capacitances of PIn/MoS_2 and PIn were 25.1 mF cm^{-2} and 3.1 mF cm^{-2}, respectively. The capacitance retention of PIn/MoS_2 was 72% of the value obtained at 0.3 mA cm^{-2}, which was closed to that of PIn (74%) but higher than those of MoS_2-based materials reported in literature, as shown in Table 1, testifying the PIn/MoS_2 nanocomposite possessed a higher rate capability.

The EIS can help us fully understand the electrochemical processes at the electrode/electrolyte interface, so EIS testing was performed using a frequency range of 0.01 Hz–100 kHz in 1.0 M H_2SO_4 solution at 0.2 V. Fig. 11A shows the Nyquist impedance spectra of PIn and PIn/MoS_2 nanocomposite. From the distinct semicircle, a charge transfer resistance (R1) of PIn/MoS_2 was 13 ohm, lower than 44 ohm of PIn. This indicated that PIn/MoS_2 nanocomposites had a superior pathway for charge transport. The equivalent circuit model with the equivalent series resistance (Rs), R1, the double layer capacitance (Cdl), Warburg (W), the parallel resistance of the leakage reaction (R2), the capacitance of active materials (C1); and the double layer capacitance (C2) of the substrate has been obtained by the simulation of the experimentally obtained EIS data using ZSimpWin software. Cyclic stability can be an important index for the performance of SCs. The results in Fig. 11B showed that PIn/MoS_2 retained over 94% of the starting value after 1000 loops, which was higher than that of PIn (91%). This indicated a high cycle stability of PIn/MoS_2 nanocomposite.

4. Conclusions

The electrochemical polymerization of indole monomer into high-quality PIn film in neutral solvents was difficult. Using

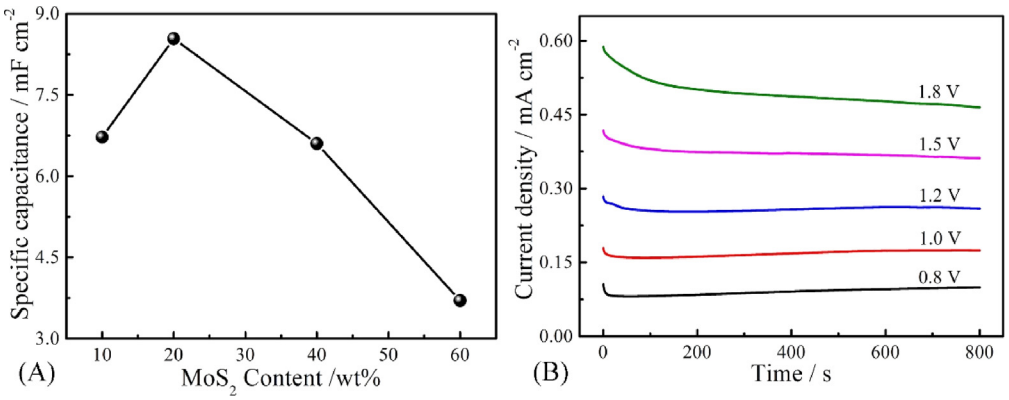

Fig. 9 (A) Specific capacitance of PIn/MoS_2 nanocomposite with different molar fraction of MoS_2; (B) Chronoamperometry curves of 50 mM indole in ACN solution containing 10 mM MoS_2 at different applied potentials for 800 s, respectively.

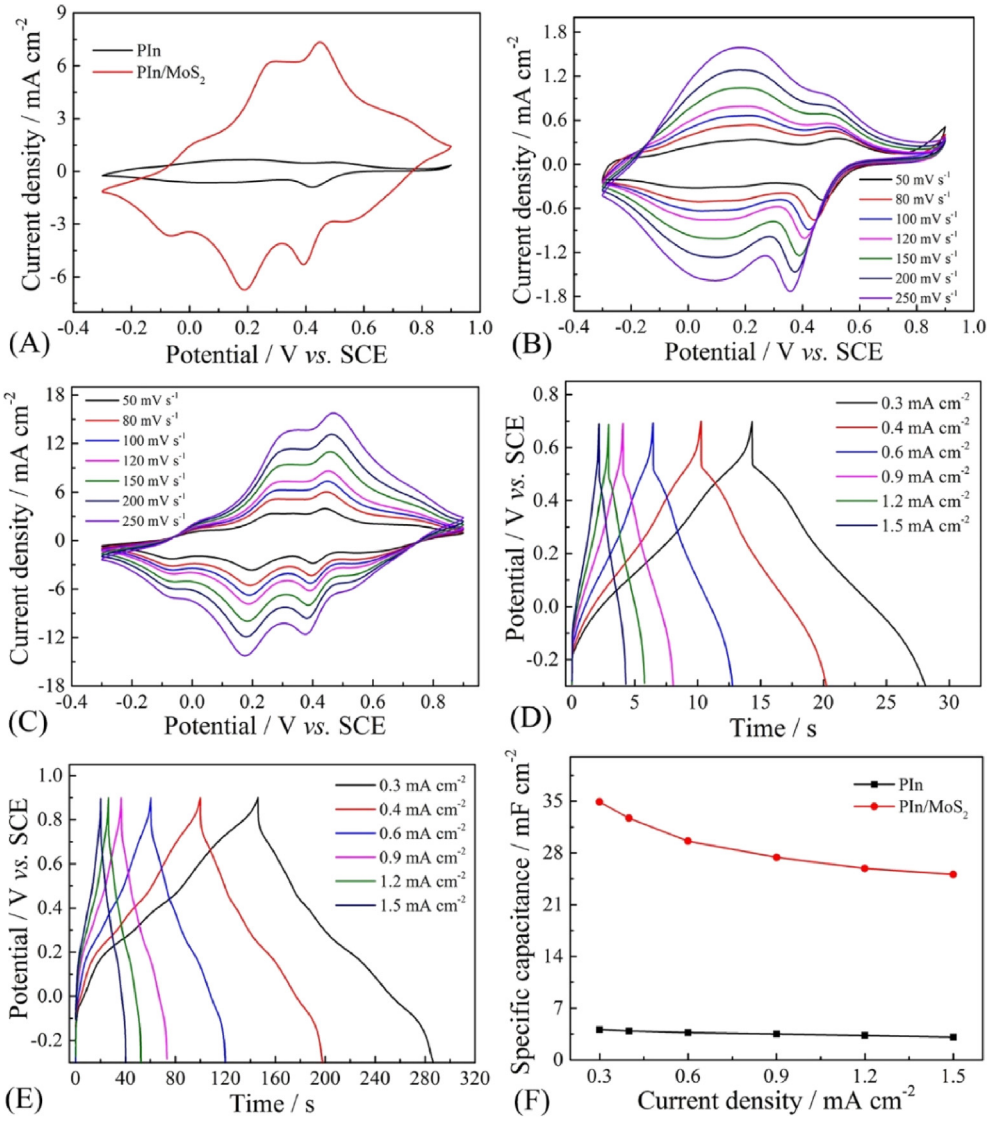

Fig. 10 The electrochemical performance of PIn and PIn/MoS_2 nanocomposite: (A) CVs at 100 mV s^{-1}, CVs of PIn (B) and PIn/MoS_2 nanocomposite (C) at different scan rates, GCD of PIn (D) and PIn/MoS_2 nanocomposite (E) at different current densities, (F) the specific capacitance as a function current density.

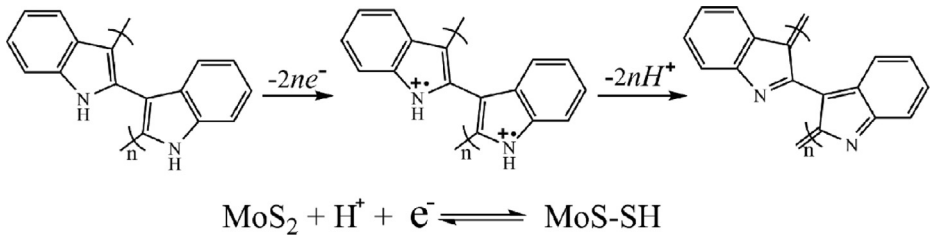

Scheme 2 The reversible faraday redox reaction of PIn and MoS_2 in 1in 1 M H_2SO_4.

Table 1 The comparison of capacitance retention of MoS_2 based materials.

Electrode materials	Test condition	Electrolytes	Capacitance retention/%	Ref
MoS_2 hierarchical nanospheres	5–50 mV s^{-1}	LiCl-PVA gel	49.5	Javed et al., 2015
Edge-oriented MoS_2 films	1–10 mA cm^{-2}	0.5 M H_2SO_4	15.1	Yang et al., 2014
sPANI/A-MoS_2	1–20 A g^{-1}	1 M H_2SO_4	62	Fu et al., 2017
MoS_2/C-3	0.5–20 A g^{-1}	1 M H_2SO_4	61.8	Ji et al., 2015
MoS_2 nanosheet	1–10 A g^{-1}	1.0 M Na_2SO_4	57.1	Huang et al., 2014
MoS_2@PANI-1	1–50 A g^{-1}	0.5 M H_2SO_4	26.9	Zhu et al. 2015
MoS_2/Cs-20	1–10 A g^{-1}	1 M Na_2SO_4	66.2	Zhang et al., 2017b
MoS_2/PPy/PANI	0.5–10 A g^{-1}	0.5 M H_2SO_4	53	Wang et al., 2016b
PIn/MoS_2	0.3–1.5 mA cm^{-2}	1 M H_2SO_4	71.9	This work

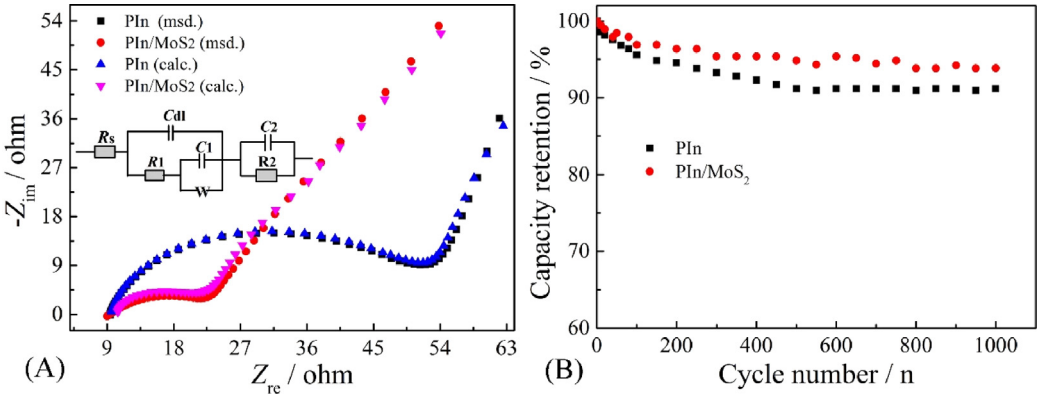

Fig. 11 Nyquist plots and fitted equivalent circuits of PIn and PIn/MoS_2 nanocomposite at 0.2 V (A) and their cycling stability at 1 mA cm^{-2} (B).

MoS_2 nanosheets as electrolytes, PIn/MoS_2 nanocomposite was firstly and easily prepared from ACN solution containing MoS_2 and indole monomer by electrochemical deposition. The onset oxidation potential of indole in ACN/MoS_2 was only 0.5 V, which was lower than that determined in ACN/$LiClO_4$ (0.75 V). The result of the morphology and structure indicated that PIn/MoS_2 nanocomposite was obtained well. The results of TGA indicated that PIn/MoS_2 nanocomposite had better thermal stability compared with those of MoS_2 and PIn. Electrochemical results indicated that PIn/MoS_2 nanocomposite had a specific capacitance of 35 mF cm^{-2} at 0.3 mA cm^{-2}, which was 8.3 times higher than that of PIn (4.2 mF cm^{-2}). After charge–discharge 1000 cycles, the capacitance retention of PIn/MoS_2 was 94% of the initial specific capacitance. Due to the formation of complexes between the monomer and the MoS_2 is beneficial to reduce the onset oxidation potential of monomer, inspired by this work, more MoS_2/CPs nanocomposites will be developed as high-performance electrode materials for supercapacitors.

Acknowledgments

This work was supported by the National Natural Science Foundation of China (Grant Nos. 51862011, 51662012, 51572117, 51762020), The Academic and Technical Leader Plan of Jiangxi Provincial Main Disciplines (20182BCB22014), Scientific Research Projects of Jiangxi Science and Technology Normal University (2016QNBJRC001).

Appendix A. Supplementary data

Supplementary data to this article can be found online at https://doi.org/10.1016/j.arabjc.2020.05.006.

References

Abthagir, P., Dhanalakshmi, K., Saraswathi, R., 1998. Thermal studies on polyindole and polycarbazole. Synth. Met. 93, 1–7.

Bazzaoui, E., Aeiyach, S., Lacaze, P., 1994. Low potential electropolymerization of thiophene in aqueous perchloric acid. J. Electroanal. Chem. 364, 63–69.

Cai, Z., Shi, X., Fan, Y., 2013. Electrochemical properties of electrospun polyindole nanofibers as a polymer electrode for lithium ion secondary battery. J. Power Sources 22, 53–59.

Cai, Z., Zhang, Q., Song, X., 2016. Improved electrochemical performance of polyindole/carbon nanotubes composite as electrode material for supercapacitors. Electron. Mater. Lett. 12, 830–840.

Cheng, Y., Zhang, Y., Jiang, H., Dong, X., Meng, C., Kou, Z., 2020. Coupled cobalt silicate nanobelt-on-nanobelt hierarchy structure with reduced graphene oxide for enhanced supercapacitive performance. J. Power Sources 448, 227407.

Delmon, B., Dallons, J., 1998. Hydrogenolysis mechanism of 5 membered heteroatom rings over MoS_2-based catalysts. Bull. Soc. Chim. Belg. 97, 475–480.

Dey, S., Matte, H., Shirodkar, S., Waghmare, U., Rao, C., 2013. Charge-transfer interaction between few-layer MoS_2 and tetrathiafulvalene. Chem.-An Asian J. 8, 1780–1784.

Fu, G., Ma, L., Gan, M., Zhang, X., Jin, M., Yang, P., Yan, M., 2017. Fabrication of 3D spongia-shaped polyaniline/MoS_2 nanospheres composite assisted by polyvinylpyrrolidone (PVP) for high-performance supercapacitors. Synth. Met. 224, 36–45.

Gan, X., Zhao, H., Quan, X., 2017. Two-dimensional MoS_2: a promising building block for biosensors. Biosens. Bioelectron. 89, 56–71.

He, P., Chen, Q., Yan, M., Xu, X., Zhou, L., Mai, L., Nan, C., 2019. Building better Zinc-ion batteries: A materials perspective. EnergyChem 100022.

Huang, F., Meng, R., Sui, Y., Wei, F., Qi, J., Meng, Q., He, Y., 2018. One-step hydrotherliumal synthesis of a CoS_2@MoS_2 nanocomposite for high-performance supercapacitors. J. Alloys Compd. 742, 844–851.

Huang, F., Yan, A., Su, Y., Wei, F., Qi, J., Meng, Q., He, Y., 2017. One-step hydrothermal synthesis of Ni_3S_4@MoS_2 nanosheet on carbon fiber paper as a binder-free anode for supercapacitor. J. Mater. Sci.: Mater Electron. 28, 12747–12754.

Huang, K., Zhang, J., Shi, G., Liu, Y., 2014. Hydrothermal synthesis of molybdenum disulfide nanosheets as supercapacitors electrode material. Electrochim. Acta 132, 397–403.

Huang, Y., Guo, Z., Liu, H., Zhang, S., Wang, P., Lu, J., Tong, Y., 2019. Heterojunction architecture of N-doped WO_3 nanobundles with Ce_2S_3 nanodots hybridized on a carbon textile enables a highly efficient flexible photocatalyst. Adv. Funct. Mater. 29, 1903490.

Javed, M., Dai, S., Wang, M., Guo, D., Chen, L., Wang, X., Hu, C., Xi, Y., 2015. High performance solid state flexible supercapacitor based on molybdenum sulfide hierarchical nanospheres. J. Power Sources 285, 63–69.

Ji, H., Liu, C., Wang, T., Chen, J., Mao, Z., Zhao, J., Hou, W., Yang, G., 2015. Porous hybrid composites of few-layer MoS_2 nanosheets embedded in a carbon matrix with an excellent supercapacitor electrode performance. Small 11, 6480–6490.

Kathiravan, D., Huang, B., Saravanan, A., Prasannan, A., Hong, P., 2019. Highly enhanced hydrogen sensing properties of sericin-induced exfoliated MoS_2 nanosheets at room temperature. Sensor. Actuat: B-Chem. 279, 138–147.

Kim, M., Kim, Y., Kim, J., Cho, S., Lee, G., Jang, J., 2016. Fabrication of a polyaniline/MoS_2 nanocomposite using self-stabilized dispersion polymerization for supercapacitors with high energy density. RSC Adv. 6, 27460–27465.

Lee, C., Yan, H., Brus, L., Heinz, T., Hone, J., Ryu, S., 2010. Anomalous lattice vibrations of single-and few-layer MoS_2. ACS nano 4, 2695–2700.

Li, D., Zhu, D., Zhou, W., Zhou, Q., Wang, T., Ye, G., Lv, L., Xu, J., 2017a. Design and electrosynthesis of monolayered MoS_2 and BF_4^--doped poly (3, 4-ethylenedioxythiophene) nanocomposites for enhanced supercapacitive performance. J. Electroanal. Chem. 801, 345–353.

Li, H., Zhang, Q., Yap, C., Tay, B., Edwin, T., Olivier, A., Baillargeat, D., 2012. From bulk to monolayer MoS_2: evolution of Raman scattering. Adv. Funct. Mater. 22, 1385–1390.

Li, K., Feng, S., Jing, C., Chen, Y., Liu, X., Zhang, Y., Zhou, L., 2019a. Assembling a double shell on a diatomite skeleton ternary complex with conductive polypyrrole for the enhancement of supercapacitors. Chem. Commun. 55, 13773–13776.

Li, K., Liu, X., Zheng, T., Jiang, D., Zhou, Z., Liu, C., Zhang, X., Zhang, Y., Losic, D., 2019b. Tuning MnO_2 to FeOOH replicas with bio-template 3D morphology as electrodes for high performance asymmetric supercapacitors. Chem. Eng. J. 370, 136–147.

Li, X., Ding, S., Xiao, X., Shao, J., Wei, J., Pang, H., Yu, Y., 2017b. N, S co-doped 3D mesoporous carbon-$Co_3Si_2O_5(OH)_4$ architectures for high-performance flexible pseudo-solid-state supercapacitors. J. Mater. Chem. A 5, 12774–12781.

Li, X., Yang, X., Xue, H., Pang, H., Xu, Q., 2020. Metal-organic frameworks as a platform for clean energy applications. EnergyChem 100027.

Maarouf, E., Billaud, D., Hannecart, E., 1994. Electrochemical cycling and electrochromic properties of polyindole. Mater. Res. Bull. 29, 637–643.

Majumder, M., Choudhary, R., Koiry, S., Thakur, A., Kumar, U., 2017. Gravimetric and volumetric capacitive performance of polyindole/carbon black/MoS_2 hybrid electrode material for supercapacitor applications. Electrochim. Acta 248, 98–111.

Mo, D., Zhou, W., Ma, X., Xu, J., 2015. Facile electrochemical polymerization of 2-(thiophen-2-yl) furan and the enhanced capacitance properties of its polymer in acetonitrile electrolyte containing boron trifluoride diethyl etherate. Electrochim. Acta 155, 29–37.

Raj, R., Ragupathy, P., Mohan, S., 2015. Remarkable capacitive behavior of a Co_3O_4–polyindole composite as electrode material for supercapacitor applications. J. Mater. Chem. A 3, 24338–24348.

Shi, G., Jin, S., Xue, G., Li, C., 1995. A conducting polymer film stronger than aluminum. Science 267, 994–996.

Shi, Y., Peng, L., Ding, Y., Zhao, Y., Yu, G., 2015. Nanostructured conductive polymers for advanced energy storage. Chem. Soc. Rev. 44, 6684–6696.

Simon, P., Gogotsi, Y., Dunn, B., 2014. Where do batteries end and supercapacitors begin?. Science 343, 1210–1211.

Snook, G., Kao, P., Best, A., 2011. Conducting-polymer-based supercapacitor devices and electrodes. J. Power Sources 196, 1–12.

Tebyetekerwa, M., Wang, X., Marriam, I., Dan, P., Zhu, M., 2017. Green approach to fabricate polyindole composite nanofibers for energy and sensor applications. Mater. Lett. 209, 400–403.

Thangappan, R., Kalaiselvam, S., Elayaperumal, A., Jayavel, R., Arivanandhan, M., Karthikeyand, R., Hayakawade, Y., 2016. Graphene decorated with MoS_2 nanosheets: a synergetic energy storage composite electrode for supercapacitor applications. Dalton Trans. 45, 2637–2646.

Ting, P., Curtis, C., Cronauer, D., 1992. Reactions of model compounds in the presence of pyrene and molybdenum sulfide (MoS_2) to simulate coprocessing. Energy Fuels 6, 511–518.

Wang, K., Li, L., Liu, Y., Zhang, C., Liu, T., 2016a. Constructing a "Pizza-like" MoS_2/polypyrrole/polyaniline ternary architecture with high energy density and superior cycling stability for supercapacitors. Adv. Mater. Interfaces 3, 1600665.

Wang, K., Xun, Q., Zhang, Q., 2020. Recent progress in metal-organic frameworks as active materials for supercapacitors. EnergyChem 2, 100025.

Wang, Q., Zhang, Y., Jiang, H., Hu, T., Meng, C., 2018. In situ generated $Ni_3Si_2O_5(OH)_4$ on mesoporous heteroatom-enriched

carbon derived from natural bamboo leaves for high-performance supercapacitors. ACS Appl. Energy Mater. 1, 3396–3409.
Wang, Q., Zhang, Y., Jiang, H., Li, X., Cheng, Y., Meng, C., 2019a. Designed mesoporous hollow sphere architecture metal (Mn Co, Ni) silicate: A potential electrode material for flexible all solid-state asymmetric supercapacitor. Chem. Eng. J. 362, 818–829.
Wang, Q., Zhang, Y., Jiang, H., Meng, C., 2019b. In-situ grown manganese silicate from biomass-derived heteroatom-doped porous carbon for supercapacitors with high performance. J. Colloid Interface Sci. 534, 142–155.
Wang, X., Zhang, Y., Zheng, J., Liu, X., Meng, C., 2019c. Hydrothermal synthesis of VS_4/CNTs composite with petal-shape structures performing a high specific capacity in a large potential range for high-performance symmetric supercapacitors. J. Colloid Interface Sci. 554, 191–201.
Wang, Y., Song, Y., Xia, Y., 2016b. Electrochemical capacitors: mechanism, materials, systems, characterization and applications. Chem. Soc. Rev. 45, 5925–5950.
Xiao, X., Zhang, G., Xu, Y., Zhang, H., Guo, X., Liu, Y., Pang, H., 2019. A new strategy for the controllable growth of MOF@PBA architectures. J. Mater. Chem. A 7, 17266–17271.
Xiao, X., Zou, L., Pang, H., Xu, Q., 2020. Synthesis of micro/-nanoscaled metal–organic frameworks and their direct electrochemical applications. Chem. Soc. Rev. 49, 301–331.
Xu, J., Nie, G., Zhang, S., Han, X., Hou, J., Pu, S., 2005. Electrosyntheses of freestanding polyindole films in boron trifluoride diethyl etherate. J. Polym. Sci. Part A: Polym. Chem. 43, 1444–1453.
Xu, J., Wang, K., Zu, S., Han, B., Wei, Z., 2010. Hierarchical nanocomposites of polyaniline nanowire arrays on graphene oxide sheets with synergistic effect for energy storage. ACS Nano 4, 5019–5026.
Yang, H., Fairbridge, C., Ring, Z., 2003. Adsorption of dibenzothiophene derivatives over a MoS_2 nanocluster a density functional theory study of structure-reactivity relations. Energy Fuels 17, 387–398.
Yang, T., Meng, L., Chen, H., Luo, S., Li, W., Jiao, K., 2016. Synthesis of thin-layered molybdenum disulfide based polyaniline nanointerfaces for enhanced direct electrochemical DNA detection. Adv. Mater. Interfaces 3, 1500700.
Yang, Y., Fei, H., Ruan, G., Xiang, C., Tour, J., 2014. Edge-oriented MoS_2 nano-porous films as flexible electrodes for hydrogen evolution reactions and supercapacitor devices. Adv. Mater. 26, 8163–8168.
Ye, K., Li, Y., Yang, H., Lia, M., Huang, Y., Zhang, S., Ji, H., 2019. An ultrathin carbon layer activated CeO_2 heterojunction nanorods for photocatalytic degradation of organic pollutants. Appl. Catal., B 259, 118085.
Zhang, G., Xiao, X., Li, B., Gu, P., Xue, H., Pang, H., 2017a. Transition metal oxides with one-dimensional/onedimensional-analogue nanostructures for advanced supercapacitors. J. Mater. Chem. A 5, 8155–8186.
Zhang, S., Hu, R., Dai, P., Yu, X., Ding, Z., Wu, M., Li, G., Ma, Y., Tu, C., 2017b. Synthesis of rambutan-like MoS_2/mesoporous carbon spheres nanocomposites with excellent performance for supercapacitors. Appl. Surf. Sci. 396, 994–999.
Zhang, Y., Jiang, H., Wang, Q., Meng, C., 2018. In-situ hydrothermal growth of $Zn_4Si_2O_7(OH)_2{\cdot}H_2O$ anchored on 3D N, Senriched carbon derived from plant biomass for flexible solid-state asymmetrical supercapacitors. Chem. Eng. J. 352, 519–529.
Zhang, Y., Liu, J., Li, S.L., Su, Z.M., Lan, Y.Q., 2019a. Polyoxometalate-based materials for sustainable and clean energy conversion and storage. EnergyChem 100021.
Zhang, Y., Wang, C., Jiang, H., Wang, Q., Zheng, J., Meng, C., 2019b. Cobalt-nickel silicate hydroxide on amorphous carbon derived from bamboo leaves for hybrid supercapacitors. Chem. Eng. J. 375, 121938.
Zhan, Y., Liu, Z., Najmaei, S., Ajayan, P., Lou, J., 2012. Large-area vapor-phase growth and characterization of MoS_2 atomic layers on a SiO_2 substrate. Small 8, 966–971.
Zheng, J., Zhang, Y., Wang, Q., Jiang, H., Liu, Y., Lv, T., Meng, C., 2018. Hydrothermally encapsulating VO_2(A) nanorods into amorphous carbon by the carbonization of glucose for energy storage device. Dalton Trans. 47, 452–464.
Zheng, S., Li, X., Yan, B., Hu, Q., Xu, Y., Xiao, X., Xue, H., Pang, H., 2017. Transition-metal (Fe Co, Ni) based metal-organic frameworks for electrochemical energy storage. Adv. Energy Mater. 7, 1602733.
Zhou, Q., Zhu, D., Ma, X., Mo, D., Jiang, F., Xu, J., Zhou, W., 2016a. PEDOT: PSS-assisted polyindole hollow nanospheres modified carbon cloth as high performance electrochemical capacitor electrodes. Electrochim. Acta 212, 662–670.
Zhou, Q., Zhu, D., Ma, X., Xu, J., Zhou, W., Zhao, F., 2016b. High-performance capacitive behavior of layered reduced graphene oxide and polyindole nanocomposite materials. RSC Adv. 6, 29840–29847.
Zhou, W., Du, Y., Zhang, H., Xu, J., Yang, P., 2010. High efficient electrocatalytic oxidation of formic acid on Pt/polyindoles composite catalysts. Electrochim. Acta 55, 2911–2917.
Zhou, W., Ma, X., Jiang, F., Zhu, D., Xu, J., Lu, B., Liu, C., 2014. Electrochemical fabrication of a porous network MnO_2/poly(5-cyanoindole) composite and its capacitance performance. Electrochim. Acta 138, 270–277.
Zhou, X., Chen, Q., Wang, A., Xu, J., Wu, S., Shen, J., 2016c. Bamboo-like composites of V_2O_5/polyindole and activated carbon cloth as electrodes for all-solid-state flexible asymmetric supercapacitors. ACS Appl. Mater. Interfaces 8, 3776–3783.
Zhu, J., Sun, W., Yang, D., Zhang, Y., Hoon, H., Zhang, H., Yan, Q., 2015. Multifunctional architectures constructing of PANI nanoneedle arrays on MoS_2 thin nanosheets for high-energy supercapacitors. Small 11, 4123–4129.